Efficient Readout of a Single Spin State in Diamond via Spin-to-Charge Conversion

B. J. Shields, Q. P. Unterreithmeier, N. P. de Leon, H. Park, and M. D. Lukin*
Department of Physics, Harvard University, Cambridge, Massachusetts 02138, USA
(Received 1 October 2014; revised manuscript received 22 February 2015; published 31 March 2015)

Efficient readout of individual electronic spins associated with atomlike impurities in the solid state is essential for applications in quantum information processing and quantum metrology. We demonstrate a new method for efficient spin readout of nitrogen-vacancy (NV) centers in diamond. The method is based on conversion of the electronic spin state of the NV to a charge-state distribution, followed by single-shot readout of the charge state. Conversion is achieved through a spin-dependent photoionization process in diamond at room temperature. Using NVs in nanofabricated diamond beams, we demonstrate that the resulting spin readout noise is within a factor of 3 of the spin projection noise level. Applications of this technique for nanoscale magnetic sensing are discussed.

DOI: 10.1103/PhysRevLett.114.136402 PACS numbers: 71.55.Cn, 03.67.-a, 07.55.Ge, 81.05.ug

The negatively charged nitrogen-vacancy (NV) center in diamond is a solid-state, atomlike impurity that combines a long lived spin-triplet ground state with an optical mechanism for both polarizing and reading out the electronic spin state at room temperature. These features make the NV center attractive for many applications such as nanoscale sensing [1–4] and quantum information processing [5–7]. While the ability to optically detect the spin state at room temperature has enabled remarkable advances in diverse areas, this readout mechanism is not perfect. Typically, single-shot optical detection of quantum states in isolated atoms and atomlike systems requires a so-called cycling transition that can scatter many photons while returning to the original state. Such cycling transitions exist at low temperature for the NV center, but at room temperature, they cannot be selectively driven by laser excitation, due to phonon broadening. Consequently, hundreds of repetitions are required to accurately distinguish between a spin prepared in $m_s = 0$ versus $m_s = 1$. While single-shot readout of the electronic spin has been observed, it is either slow (as in the case of repetitive readout involving nuclear ancilla [8,9]) or requires cryogenic temperatures [10].

It is well known that the NV center can exist in several charge states. In addition to NV^-, the neutral charge state (NV^0) has attracted recent interest for superresolution microscopy [11–14]. Photoionization between the two charge states is well established [15,16]. However, previous studies of the charge-state dynamics have focused on ionization time scales that are much longer than the internal dynamics of the NV^- energy levels, specifically, the lifetime of the metastable singlet state. Studies in this regime have established the charge state as a stable and high-contrast degree of freedom for fluorescence imaging but have not explored the effect of spin on ionization. In this Letter, we investigate photoionization on time scales relevant to the singlet-state dynamics. In this regime, we demonstrate a method for spin-to-charge conversion (SCC) that can be used for fast, efficient readout of the electronic spin state of the NV center.

The key component of the SCC method is a two-step pulse sequence that rapidly transfers the spin state of NV^- to a charge distribution, as illustrated in Fig. 1. This mechanism is related to the well-established technique for optically detected magnetic resonance [17], in that it takes advantage of the spin-dependent shelving process to

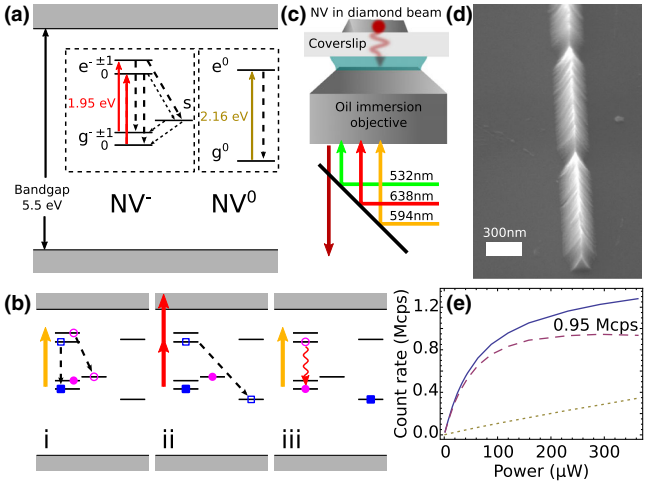

FIG. 1 (color online). SCC measurement idea. (a) NV center level diagram, indicating triplet ground (g^-), excited (e^-), and metastable singlet (s) states of NV^- and ground (g^0) and excited (e^0) states of NV^0. (b) SCC measurement process for an initial state of $m_s = 0$ (blue squares) or $m_s = 1$ (pink circles). (i) A 594-nm pulse either shelves into the singlet state ($m_s = 1$) or cycles ($m_s = 0$). (ii) A 638-nm pulse rapidly ionizes the NV^- triplet states to NV^0. (iii) Single-shot charge-state measurement with 594-nm light. (c) Setup for high collection efficiency from nanobeams. (d) SEM micrograph of a nanobeam transferred to silicon (60° tilt). (e) Saturation fluorescence measurement. Total fluorescence (blue line), background (gold dotted line), and NV signal (red dashed line). The maximum count rate is 0.945 Mcps after background subtraction.

the metastable singlet state. Specifically, we utilize the fact that, upon 594-nm excitation, the $m_s = \pm 1$ states of NV^- can be optically shelved into a metastable singlet manifold via an intersystem crossing, while the $m_s = 0$ state cycles within the manifold of triplet ground and excited states. Subsequently, the NV^- triplet excited state can be ionized using a second, intense pulse of 638-nm light, but the NV^- singlet manifold cannot be excited back to the triplet excited state by either 594- or 638-nm light and hence is protected from ionization. Thus, NV^- in the $m_s = 0$ state will be ionized to NV^0 upon two-pulse excitation, whereas NV^- in the $m_s = \pm 1$ state will remain mostly as NV^-. Single-shot charge-state detection then provides a sensitive measurement of the electron spin state. The stability and spectral contrast of the charge states minimize the contribution of photon shot noise, so that the measurement is instead limited by the SCC efficiency. As a result, the readout noise is dramatically reduced, to a limit of ~2.76 times the spin projection noise level.

For our measurements we use naturally occurring NVs in type IIa chemical vapor deposition grown diamond (Element6). To enhance the photon collection efficiency, we carve the diamond into nanobeams and transfer them to a glass coverslip for imaging in a confocal microscope [Fig. 1(c)]. We fabricate nanobeams with an angled reactive ion etch [18] that yields triangular cross-section waveguides of 300-nm width and 20-μm length, suspended above the diamond substrate. In the same step, we etch notches (50-nm depth) every 2 μm along the beam, to scatter waveguided light. Using a 500-nm radius, piezo-controlled tungsten tip, we detach the beams, place them on the coverslip, and orient them with the smooth, unetched diamond surface contacting the glass.

To address the NV optically, we illuminate it through an oil-immersion objective (Nikon, NA = 1.49) with laser light at 532-, 594-, and 638-nm wavelengths [Fig. 1(c)], which pump the charge state into NV^-, drive NV^- to the triplet excited state, and ionize from the NV^- triplet manifold to NV^0, respectively. Acousto-optic modulators control the timing and intensity of each laser. We collect NV fluorescence through the same objective and image it onto a multimode fiber.

Recent work on high collection efficiency with immersion imaging systems relied upon the placement of an emitter in a low-index layer on top of a high-index substrate [19,20]. Because of the high refractive index of diamond ($n_{\mathrm{diamond}} = 2.4$), however, obtaining a substrate of higher index is difficult. Instead, we use the subwavelength dimension of the nanobeams to avoid total internal reflection at the diamond surface, efficiently coupling the NV fluorescence to radiative modes in the glass. In this way we observe a maximum count rate of 9.45×10^5 counts per second (cps) under cw 532-nm illumination [Fig. 1(e)]. To manipulate the NV^- electron spin sublevels, we align the magnetic field from a permanent magnet with the NV axis, splitting $m_s = \pm 1$. A proximal copper wire (25-μm diameter) delivers a 2.917-GHz microwave field to drive transitions between $m_s = 0$ and $m_s = 1$.

Central to our spin readout process is a mechanism for high-fidelity measurement of the NV charge state [15]. This measurement utilizes the different excitation and emission spectra for NV^- and NV^0, allowing for efficient spectral discrimination. A low power of 594-nm light efficiently excites the NV^- sideband but only weakly excites NV^0 [Fig. 2(a)]. A 655-nm long-pass filter in the collection path eliminates residual NV^0 fluorescence. In this way, NV^- is 20–30 times brighter than NV^0 (depending on laser intensity [21], yielding a high-contrast measurement.

Laser illumination also causes the NV to jump between charge states [15]. The NV first absorbs one photon and then, while in an excited configuration, absorbs a second photon, either exciting an electron to the conduction band to ionize NV^- to NV^0 or recapturing an electron from the valence band to convert NV^0 to NV^-. At low power, the ionization and recapture rates g_{-0} and g_{0-}, respectively, obey a quadratic power dependence, whereas the NV^0 and NV^- photon count rates γ_0 and γ_- obey a linear power dependence [15]. Consequently, illumination power and integration time can be adjusted to allow faster readout at the expense of lower fidelity. Here we define the charge-state readout fidelity to be

$$\mathcal{F}_C = \frac{1}{2}(\mathcal{F}_0 + \mathcal{F}_-), \tag{1}$$

where $\mathcal{F}_0$ and $\mathcal{F}_-$ are the probabilities to correctly determine the NV^0 and NV^- charge states, respectively.

To characterize $\mathcal{F}_C$ for our setup, we measure $g_{0-,-0}$ and $\gamma_{0,-}$ under cw 594-nm illumination, for powers between 0.875 and 15 μW. At each power P, we record the number of photons detected in a time window $t \sim 1/g_{-0}$. We fit the photon number distribution for 100 000 time windows with a model for the charge-state dynamics, to obtain $g_{0-,-0}(P)$ and $\gamma_{0,-}(P)$ [21]. From the measured rates, we calculate the optimal readout time t_R to maximize $\mathcal{F}_C(P)$ [Fig. 2(b)]. We obtain high fidelity ($\mathcal{F}_C \sim 0.9$) even for t_R as short as 10 μs.

A similar measurement scheme rapidly initializes the NV into NV^-. To initialize, we apply a short, high power pump pulse of 532-nm light (150 ns at 300 μW), then measure the charge state with a short probe pulse of 594-nm light ($t_{\mathrm{probe}} = 900$ ns at 11 μW). In this regime, $g_{-0} t_{\mathrm{probe}} \ll 1$, making ionization unlikely. Detection of $n_{\mathrm{probe}} \geq 1$ photons verifies that the final charge state is NV^-. Failed verification attempts ($n_{\mathrm{probe}} = 0$) can be discarded, so that the initialization fidelity is simply $\mathcal{F}_I = p(\mathrm{NV}^- | n_{\mathrm{probe}} \geq 1)$.

To verify $\mathcal{F}_I$, we perform a pump-probe combination followed by charge readout at low power. The readout photon number distribution is shown in Figs. 2(d) and 2(e). Figure 2(d) shows results for all probe outcomes, indicating an initialization fidelity of 0.723 ± 0.006. Figure 2(e) shows the distribution conditioned on detection of one or more probe photons, for which the fidelity increases to

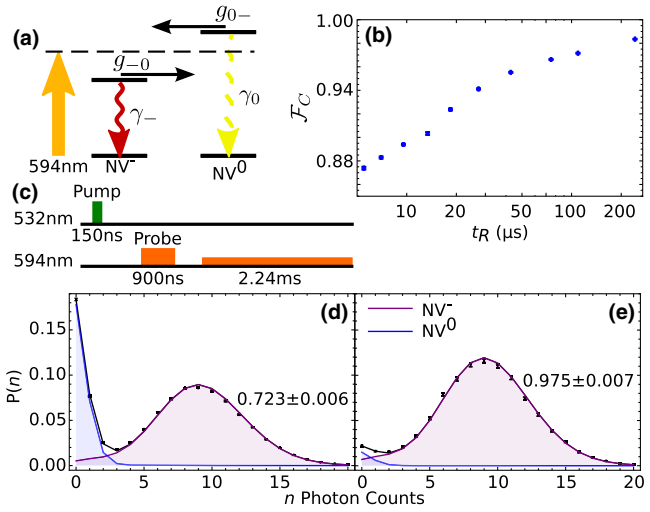

FIG. 2 (color online). Charge-state initialization and readout. (a) Level diagram for charge readout. 594-nm light efficiently excites NV^-, while weakly exciting NV^0, yielding photon count rates γ_- and γ_0, respectively. Ionization occurs from the excited states at rates g_{-0} and g_{0-}. (b) Optimized charge-state readout fidelity $\mathcal{F}_C(t_R)$, determined by measuring γ_-, γ_0, g_{-0}, and g_{0-} at various illumination intensities. (c) Pulse sequence for charge initialization. A pump-probe sequence initializes into NV^- (see the text), and a $t_R = 2.24$ms readout (594 nm, 820 nW) verifies the charge state. (d) The readout photon number distribution for 100 000 iterations indicates an initialization fidelity of 0.723 ± 0.006. The longer-than-optimal t_R ensures an accurate fit of the populations, but here we plot the distribution for the first 240 μs for clarity. (e) Conditioning on one or more probe photons, the fidelity increases to 0.975 ± 0.007. The black line is a fit to the full 2.24-ms readout. The blue and purple lines indicate NV^0 and NV^- contributions, respectively.

0.975 ± 0.007. For these pump-probe conditions, the success probability is $p(n_{\text{probe}} \geq 1) = 0.216 \pm 0.001$.

We next demonstrate spin-dependent control of the ionization dynamics, allowing for efficient conversion from the NV^- electron spin state to a charge distribution. We first initialize into NV^- and prepare the spin into either $m_s = 1$ or $m_s = 0$, then apply a short, intense pulse of 594-nm light (145 μW) that drives NV^- into its triplet excited state [Fig. 1(b)i]. Depending on initial spin-state preparation, the triplet excited state either decays into the singlet state via an intersystem crossing ($m_s = 1$) or relaxes back to the triplet ground state ($m_s = 0$). Following the 594-nm shelving pulse, we immediately apply a short, high power pulse of 638-nm light (22.5 mW) to rapidly ionize any population remaining in the triplet manifold [Fig. 1(b)ii]. This pulse does not excite the singlet manifold of NV^-, leading to spin-dependent ionization and thus spin-to-charge conversion. Finally, we measure the charge state [Fig. 1(b)iii].

The resulting photon number distributions are shown in Fig. 3(b), for initial spin states $m_s = 0$ (top) and $m_s = 1$ (bottom), where we use shelving pulse duration $t_{\text{shelf}} = 60$ ns and ionization pulse duration $t_{\text{ion}} = 20$ ns. From a fit to the measured photon number distributions, we determine the average population in NV^- after the SCC step. For an initial state of $m_s = 0$ or $m_s = 1$, we label the average final NV^- population β_0 or β_1. The contrast between β_0 and β_1 characterizes the efficiency of the SCC mechanism. To optimize SCC efficiency, we sweep t_{shelf} and t_{ion}, as shown in Figs. 3(c) and 3(d). In Fig. 3(c), t_{shelf} is fixed at 60 ns and we sweep t_{ion}. For each t_{ion}, we measure the photon number distributions as in Fig. 3(b) to find $\beta_{0,1}(t_{\text{ion}})$. Similarly, in Fig. 3(d), we fix $t_{\text{ion}} = 20$ ns and sweep t_{shelf}. As t_{shelf} increases, the $m_s = 1$ population is transferred to the singlet state and protected from ionization, resulting in a maximum for $\beta_1(t_{\text{shelf}})$ at $t_{\text{shelf}} = 60$ ns.

To quantify the performance of the SCC mechanism for NV^- electronic spin readout, we consider its applications for magnetometry [24]. We consider a Hahn echo [25] magnetometry sequence and compare the readout noise for the SCC scheme to a conventional optically detected magnetic resonance readout. In both cases the magnetic field sensitivity is

$$\eta = (\pi\hbar/2g\mu_B) \times \sigma_R \times \sqrt{(\tau + t_I + t_R)/\tau^2}, \qquad (2)$$

where g is the electron gyromagnetic ratio, μ_B is the Bohr magneton, τ is the Hahn echo time, t_I is the initialization time, and t_R is the readout time. σ_R is a measure of the spin readout noise for a single measurement, normalized so $\sigma_R = 1$ for a perfect measurement (limited by only spin projection noise). It is important to note that, for SCC readout, both σ_R and the measurement duty cycle depend

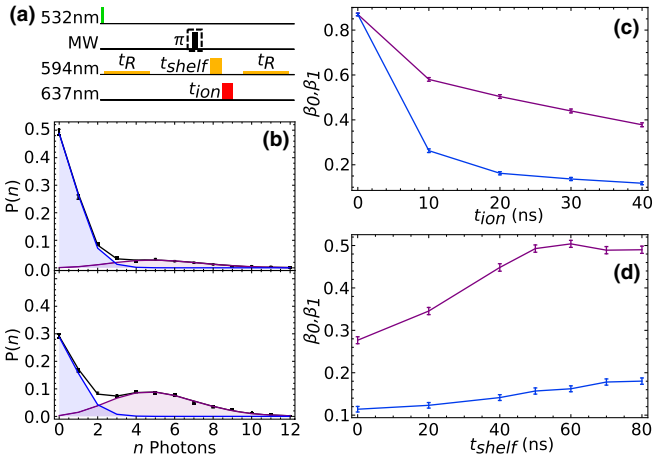

FIG. 3 (color online). Spin-to-charge conversion. (a) Pulse sequence consisting of initialization (40-ns, 300-μW pump; 500-μs, 500-nW probe), followed by microwave (MW) manipulation to prepare in $m_s = 0$ or $m_s = 1$, two-pulse SCC for duration t_{shelf} and t_{ion}, and finally charge readout (500μs, 500 nW). (b) Photon number distributions for $t_{\text{shelf}} = 60$ ns and $t_{\text{ion}} = 20$ ns. An initial $m_s = 0$ state ionizes to NV^0 (top, $\beta_0 = 0.162 \pm 0.007$) while $m_s = 1$ is shelved into the singlet state and protected from ionization (bottom, $\beta_1 = 0.504 \pm 0.009$). (c) Final NV^- population for t_{ion} between 0 and 40 ns ($t_{\text{shelf}} = 60$ns). (d) Final NV^- population for t_{shelf} between 0 and 80 ns ($t_{\text{ion}} = 20$ ns), showing dynamics of the shelving process.

on t_R, so the optimal readout conditions depend on τ. This is in contrast to conventional readout, for which the readout adds a fixed overhead time to the measurement.

In the conventional readout scheme, the NV is prepared into NV^-, the Hahn echo is applied for time τ, and the spin is read out with a short excitation pulse (typically ~200 ns of 532-nm light), during which time an average number of photons α_0 or α_1 is counted when the NV is projected into $m_s = 0$ or $m_s = 1$, respectively. The two sources of noise are spin projection noise and photon shot noise, and the overall readout noise is [24]

$$\sigma_R = \sqrt{1 + 2(\alpha_0 + \alpha_1)/(\alpha_0 - \alpha_1)^2}. \quad (3)$$

For a bulk diamond sample, typical photon collection efficiencies result in $\sigma_R \sim 20$ [26]. With the enhanced collection efficiency from the nanobeam geometry, we observe $\alpha_0 = 0.238 \pm 0.001$ and $\alpha_1 = 0.154 \pm 0.002$, resulting in $\sigma_R = 10.6 \pm 0.3$. In both cases, photon shot noise is by far the dominant source of noise.

In the SCC readout method, on the other hand, the final charge state is measured by counting photons and assigning an NV^0 or NV^- result based on a threshold photon number. The probability of measuring NV^- in this way is $\tilde{\beta}_0$ or $\tilde{\beta}_1$ for an initial spin state of $m_s = 0$ or $m_s = 1$, and the spin readout noise is given by

$$\sigma_R^{\mathrm{SCC}} = \sqrt{(\tilde{\beta}_0 + \tilde{\beta}_1)(2 - \tilde{\beta}_0 - \tilde{\beta}_1)/(\tilde{\beta}_0 - \tilde{\beta}_1)^2}. \quad (4)$$

In the limit of perfect charge readout, $\tilde{\beta}_{0,1}$ approach the true charge-state populations $\beta_{0,1}$. For the optimized SCC process in Fig. 3(b), this corresponds to $\sigma_{R,\mathrm{min}}^{\mathrm{SCC}} = 2.76 \pm 0.09$. Note that this includes the effects of imperfect initial spin polarization (measured to be $92\% \pm 1\%$ in our system [21]) and imperfect charge initialization.

To evaluate the practical utility of SCC readout for magnetometry, however, it is important to know how σ_R^{SCC} depends on t_R. We measure $\sigma_R^{\mathrm{SCC}}(t_R)$ using the pulse sequence shown in Fig. 4(a) (inset), with the fast initialization scheme described above ($t_I = 6.5$ μs), over a range of values for t_R. We optimize the readout power and threshold photon number for each t_R to minimize $\sigma_R^{\mathrm{SCC}}(t_R)$. The results are shown in Fig. 4(a). For short $t_R \sim 5$ μs, $\sigma_R^{\mathrm{SCC}}(t_R)$ provides a modest improvement over the conventional readout scheme. For longer t_R, the contribution from photon shot noise during charge readout diminishes, yielding a threefold improvement over conventional readout. This measurement contains the complete information necessary to tune the SCC readout time for a particular spin measurement.

With the measurement of $\sigma_R^{\mathrm{SCC}}(t_R)$, we estimate the magnetometer sensitivity directly from Eq. (2), as shown in Fig. 4(b). For the spin coherence times measured in our nanobeams (200 μs [21]), we estimate a sensitivity of 4 $\mathrm{nT/Hz^{1/2}}$, while for coherence times in the range of

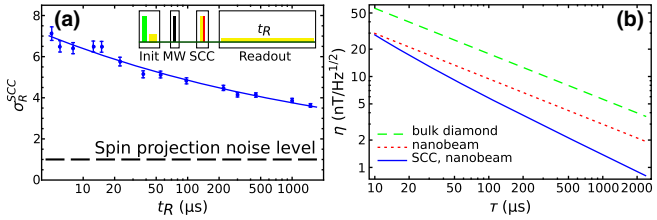

FIG. 4 (color online). Time dependence and magnetometer sensitivity. (a) Measurement of a $\sigma_R^{\mathrm{SCC}}(t_R)$ (blue points) power law fit (solid line). The inset shows the pulse sequence, consisting of initialization (150-ns, 300-μW pump; 900-ns, 11-μW probe), microwave pulse to prepare $m_s = 0$ or $m_s = 1$, SCC sequence (50-ns, 135-μW shelving pulse; 30-ns, 7.1-mW ionization pulse), and readout. (b) Based on the fit in (a), we directly calculate the magnetometer sensitivity [Eq. (2)] for SCC readout (blue solid line). The sensitivity for conventional readout in bulk diamond ($\sigma_R = 20$, green dashed curve) and diamond nanobeams ($\sigma_R = 10.6$, red dotted curve) is shown for comparison.

2 ms, demonstrated in ^{12}C isotopically pure diamond [26], the sensitivity will be 900 $\mathrm{pT/Hz^{1/2}}$. While the benefits diminish for very short spin coherence times, we expect the method to find applicability even in the case of near-surface NVs with spin coherence times down to ~20 μs [27].

Before concluding, we note that several improvements to the SCC method may be possible. We expect $\sigma_R^{\mathrm{SCC}}(t_R)$ to approach $\sigma_{R,\mathrm{min}}^{\mathrm{SCC}}$ for long t_R, as photon shot noise becomes negligible. However, the measured values are somewhat higher. We believe this is due to the pump duty cycle employed for fast initialization, which may affect the ionization dynamics in a way not fully described by our model. Additionally, the limiting value $\sigma_{R,\mathrm{min}}^{\mathrm{SCC}}$ depends on the internal dynamics of NV^- and the photoionization cross section, which is material dependent. For instance, the photoionization behavior in diamond with high defect density can be very different from that observed here, with the charge state being much less stable [16]. Therefore, it may be possible to obtain more favorable ionization dynamics and thereby a lower value for $\sigma_{R,\mathrm{min}}^{\mathrm{SCC}}$, by controlling the defect density in the crystal.

To summarize, we have studied the ionization dynamics of the NV center on time scales commensurate with the internal spin dynamical processes of the NV^- charge state. In particular, we have demonstrated a spin-dependent ionization process that maps the spin state of NV^- onto a charge distribution between NV^- and NV^0. This mechanism significantly improves the spin readout noise of a single measurement shot, to a limit of ~2.76 times the spin projection noise level. This directly results in improved single spin magnetometer sensitivity. In addition to applications in nanoscale sensing, the selective ionization of the NV^- triplet manifold can be used to extend ionization-based studies of NV spectroscopy [15].

We thank A. Gali, A. Trifonov, S. Kolkowitz, A. Sipahigil, T. Tiecke, Y. Chu, and A. Zibrov for helpful discussions and experimental support. This work was

performed in part at the Harvard Center for Nanoscale Systems. We acknowledge support from the NSF, CUA, HQOC, DARPA QuASAR program, ARO MURI, AFOSR MURI, and the Moore Foundation.

*lukin@physics.harvard.edu

[1] G. Balasubramanian, I. Y. Chan, R. Kolesov, M. Al-Hmoud, J. Tisler, C. Shin, C. Kim, A. Wojcik, P. R. Hemmer, A. Krueger, T. Hanke, A. Leitenstorfer, R. Bratschitsch, F. Jelezko, and J. Wrachtrup, Nanoscale imaging magnetometry with diamond spins under ambient conditions, Nature (London) **455**, 648 (2008).

[2] J. R. Maze, P. L. Stanwix, J. S. Hodges, S. Hong, J. M. Taylor, P. Cappellaro, L. Jiang, M. V. G. Dutt, E. Togan, A. S. Zibrov, A. Yacoby, R. L. Walsworth, and M. D. Lukin, Nanoscale magnetic sensing with an individual electronic spin in diamond, Nature (London) **455**, 644 (2008).

[3] G. Kucsko, P. C. Maurer, N. Y. Yao, M. Kubo, H. J. Noh, P. K. Lo, H. Park, and M. D. Lukin, Nanometre-scale thermometry in a living cell, Nature (London) **500**, 54 (2013).

[4] D. M. Toyli, C. F. de las Casas, D. J. Christle, V. V. Dobrovitski, and D. D. Awschalom, Fluorescence thermometry enhanced by the quantum coherence of single spins in diamond, Proc. Natl. Acad. Sci. U.S.A. **110**, 8417 (2013).

[5] P. Neumann, R. Kolesov, B. Naydenov, J. Beck, F. Rempp, M. Steiner, V. Jacques, G. Balasubramanian, M. L. Markham, D. J. Twitchen, S. Pezzagna, J. Meijer, J. Twamley, F. Jelezko, and J. Wrachtrup, Quantum register based on coupled electron spins in a room-temperature solid, Nat. Phys. **6**, 249 (2010).

[6] M. V. G. Dutt, L. Childress, L. Jiang, E. Togan, J. Maze, F. Jelezko, A. S. Zibrov, P. R. Hemmer, and M. D. Lukin, Quantum register based on individual electronic and nuclear spin qubits in diamond, Science **316**, 1312 (2007).

[7] T. van der Sar, Z. H. Wang, M. S. Blok, H. Bernien, T. H. Taminiau, D. M. Toyli, D. A. Lidar, D. D. Awschalom, R. Hanson, and V. V. Dobrovitski, Decoherence-protected quantum gates for a hybrid solid-state spin register, Nature (London) **484**, 82 (2012).

[8] L. Jiang, J. S. Hodges, J. R. Maze, P. Maurer, J. M. Taylor, D. G. Cory, P. R. Hemmer, R. L. Walsworth, A. Yacoby, A. S. Zibrov, and M. D. Lukin, Repetitive readout of a single electronic spin via quantum logic with nuclear spin ancillae, Science **326**, 267 (2009).

[9] P. Neumann, J. Beck, M. Steiner, F. Rempp, H. Fedder, P. R. Hemmer, J. Wrachtrup, and F. Jelezko, Single-shot readout of a single nuclear spin, Science **329**, 542 (2010).

[10] L. Robledo, L. Childress, H. Bernien, B. Hensen, P. F. A. Alkemade, and R. Hanson, High-fidelity projective read-out of a solid-state spin quantum register, Nature (London) **477**, 574 (2011).

[11] K. Y. Han, S. K. Kim, C. Eggeling, and S. W. Hell, Metastable dark states enable ground state depletion microscopy of nitrogen vacancy centers in diamond with diffraction-unlimited resolution, Nano Lett. **10**, 3199 (2010).

[12] K. Y. Han, D. Wildanger, E. Rittweger, J. Meijer, S. Pezzagna, S. W. Hell, and C. Eggeling, Dark state photophysics of nitrogen vacancy centres in diamond, New J. Phys. **14**, 123002 (2012).

[13] G. Waldherr, J. Beck, M. Steiner, P. Neumann, A. Gali, T. Frauenheim, F. Jelezko, and J. Wrachtrup, Dark States of Single Nitrogen-Vacancy Centers in Diamond Unraveled by Single Shot NMR, Phys. Rev. Lett. **106**, 157601 (2011).

[14] K. Beha, A. Batalov, N. B. Manson, R. Bratschitsch, and A. Leitenstorfer, Optimum Photoluminescence Excitation and Recharging Cycle of Single Nitrogen-Vacancy Centers in Ultrapure Diamond, Phys. Rev. Lett. **109**, 097404 (2012).

[15] N. Aslam, G. Waldherr, P. Neumann, F. Jelezko, and J. Wrachtrup, Photo-induced ionization dynamics of the nitrogen vacancy defect in diamond investigated by single-shot charge state detection, New J. Phys. **15**, 013064 (2013).

[16] N. Manson and J. Harrison, Photo-ionization of the nitrogen-vacancy center in diamond, Diam. Relat. Mater. **14**, 1705 (2005).

[17] A. Gruber, A. Dräbenstedt, C. Tietz, L. Fleury, J. Wrachtrup, and C. v. Borczyskowski, Scanning confocal optical microscopy and magnetic resonance on single defect centers, Science **276**, 2012 (1997).

[18] M. J. Burek, N. P. de Leon, B. J. Shields, B. J. M. Hausmann, Y. Chu, Q. Quan, A. S. Zibrov, H. Park, M. D. Lukin, and M. Lončar, Free-standing mechanical and photonic nanostructures in single-crystal diamond, Nano Lett. **12**, 6084 (2012).

[19] K. G. Lee, X. W. Chen, H. Eghlidi, P. Kukura, R. Lettow, A. Renn, V. Sandoghdar, and S. Gotzinger, A planar dielectric antenna for directional single-photon emission and near-unity collection efficiency, Nat. Photonics **5**, 166 (2011).

[20] D. Riedel, D. Rohner, M. Ganzhorn, T. Kaldewey, P. Appel, E. Neu, R. J. Warburton, and P. Maletinsky, Low-Loss Broadband Antenna for Efficient Photon Collection from a Coherent Spin in Diamond, Phys. Rev. Applied **2**, 064011 (2014).

[21] See Supplemental Material at http://link.aps.org/supplemental/10.1103/PhysRevLett.114.136402 for additional details regarding experimental setup and diamond nanobeams, photon statistics modeling and measurement of ionization rates, optimization of readout noise, and measurement of initial electron spin polarization, which includes Refs. [22,23].

[22] L. Childress, M. V. Gurudev Dutt, J. M. Taylor, A. S. Zibrov, F. Jelezko, J. Wrachtrup, P. R. Hemmer, and M. D. Lukin, Coherent dynamics of coupled electron and nuclear spin qubits in diamond, Science **314**, 281 (2006).

[23] L. Robledo, H. Bernien, T. van der Sar, and R. Hanson, Spin dynamics in the optical cycle of single nitrogen-vacancy centres in diamond, New J. Phys. **13**, 025013 (2011).

[24] J. M. Taylor, P. Cappellaro, L. Childress, L. Jiang, D. Budker, P. R. Hemmer, A. Yacoby, R. Walsworth, and M. D. Lukin, High-sensitivity diamond magnetometer with nanoscale resolution, Nat. Phys. **4**, 810 (2008).

[25] E. L. Hahn, Spin echoes, Phys. Rev. **80**, 580 (1950).

[26] G. Balasubramanian, P. Neumann, D. Twitchen, M. Markham, R. Kolesov, N. Mizuochi, J. Isoya, J. Achard, J. Beck, J. Tissler, V. Jacques, P. R. Hemmer, F. Jelezko, and J. Wrachtrup, Ultralong spin coherence time in isotopically engineered diamond, Nat. Mater. **8**, 383 (2009).

[27] M. Loretz, S. Pezzagna, J. Meijer, and C. L. Degen, Nanoscale nuclear magnetic resonance with a 1.9-nm-deep nitrogen-vacancy sensor, Appl. Phys. Lett. **104**, 033102 (2014).